Sensors & Diagnostics

PAPER

View Article Online
View Journal | View Issue

Cite this: *Sens. Diagn.*, 2026, **5**, 56

Label-free optical detection of miRNA using electrostatic interactions between oppositely charged gold nanoparticles for signal amplification

Fatemeh Hakimian,[a] Behdad Delavari,[b] Samaneh Hadian-Ghazvini,[a] Mohammad Behnam Rad,[a] Fariba Dashtestani,[a] Vahid Sheikhhassani,[c] Hamideh Fouladiha,[d] Hadi Zare-Zardini[e] and Hedayatollah Ghourchian *[a]

We developed a simple yet innovative biosensing system for the detection of miRNA-155 (miR-155), a promising biomarker for the early diagnosis of breast cancer. This system utilizes two types of gold nanoparticles (Au NPs) with opposing surface charges: (1) negatively charged citrate-stabilized Au NPs (Cit-Au NPs) for probe immobilization and (2) positively charged polyethylenimine-capped Au NPs (PEI-Au NPs) for signal amplification. The DNA probe was covalently attached to Cit-Au NPs *via* Au–S bonds. In the presence of miR-155, a DNA–miRNA hybrid forms, stabilizing the nanoparticles. The subsequent introduction of PEI-Au NPs enhances the surface plasmon resonance (SPR) signal due to increased nanoparticle dispersion. PEI-Au NPs enhance the diagnostic system's sensitivity by providing a high surface area and improved nanoparticle stability. Upon binding to the DNA–miRNA hybrid, the increased interparticle distance leads to enhanced colloidal stability. This stabilization manifests visually as an intensified red color, indicating the presence of the target when PEI-Au NPs are introduced into the solution. In contrast, in the absence of miR-155, electrostatic interactions cause aggregation of the Au NPs, leading to a measurable SPR shift. This facile method demonstrated a detection limit of approximately 8 pM and a wide linear detection range from 80 pM to 2 μM, making it a promising tool for early diagnostics of breast cancer.

Received 16th July 2025,
Accepted 25th September 2025

DOI: 10.1039/d5sd00129c

rsc.li/sensors

1. Introduction

Breast cancer, the second most prevalent malignancy globally, remains a complex disease with steadily rising incidence rates and persistently high mortality, despite significant advances in screening and treatment protocols.[1–4] Often referred to as the "modern epidemic of the 21st century",[5] early detection is paramount for improving treatment outcomes and reducing mortality.[6] Mammography, the current gold standard for screening, is constrained by a high false-positive rate and substantial economic burden,[6] underscoring the urgent need for alternative methods capable of more accurately distinguishing malignant from benign lesions.[6]

Circulating biomarkers like cancer antigen 27-29 (CA27-29) and carcinoembryonic antigen (CEA) have been explored, but they lack sufficient sensitivity for early breast cancer detection.[6] In contrast, microRNAs (miRNAs) —small, single-stranded, non-coding RNAs 18–25 nucleotides in length[9,10]— have emerged as highly promising candidates due to their critical roles in tumorigenesis, tissue-specific expression profiles, and detectable presence in biofluids.[7–9] Among these, miRNA-155 (miR-155) has been consistently identified in multiple studies as a potential diagnostic and prognostic biomarker for breast cancer.[11,12]

Traditional miRNA detection methods—including RNA sequencing, microarray analysis, northern blotting, and quantitative real-time PCR (qRT-PCR)—are technically robust and reliable, but they are limited by high equipment costs, limited portability, and prolonged processing times.[7,13] These challenges limit their application, particularly in point-of-care (POC) settings and resource-limited regions,[7] thus driving

[a] *Institute of Biochemistry and Biophysics, University of Tehran, Tehran, Iran. E-mail: Ghourchian@ut.ac.ir*
[b] *School of Biomedical Science, Faculty of Medicine and Health, University of New South Wales, 2052 NSW, Australia*
[c] *Medical Systems Biophysics and Bioengineering, Division of Systems Pharmacology and Pharmacy, Leiden Academic Centre for Drug Research, Leiden University, Leiden, The Netherlands*
[d] *Department of Biotechnology, College of Science, University of Tehran, Tehran, Iran*
[e] *Department of Biomedical Engineering, Meybod University, Meybod, Iran*

demand for rapid, cost-effective, portable, and highly sensitive alternatives.

Sensor-based devices have been developed to address these needs, offering enhanced speed and portability. However, detection sensitivity often remains inadequate. The integration of nanomaterials into biosensor designs has enhanced sensitivity and specificity, leveraging their size-dependent properties and biomolecular-scale dimensions.[14,15] Nevertheless, technical challenges, the experimental-stage status of many technologies, and the prohibitive costs of advanced nanomaterials continue to hinder widespread commercialization.[15]

Among the biosensing modalities, colorimetric assays have gained considerable attention due to their strong translational potential, owing to their operational simplicity, low cost, and minimal dependence on sophisticated instrumentation.[15,16] Gold nanoparticles (Au NPs) are extensively employed in colorimetric biosensing due to their exceptional optical and surface properties, including high extinction coefficients, tunable localized surface plasmon resonance (LSPR), and facile surface functionalization.[16–19] In aqueous solution, Au NPs exhibit an LSPR peak near 520 nm, giving rise to their characteristic red-wine color.[16]

Au NP aggregation induces dipole–dipole interactions and interparticle LSPR coupling, resulting in a shift of the plasmon resonance and a visible color transition from red to purple, blue, or pale pink.[18,20] Two primary Au NP-based colorimetric detection strategies are cross-linking and non-cross-linking aggregation. In cross-linking aggregation, pioneered by Mirkin's group, a target DNA oligonucleotide bridges two types of Au NPs functionalized with complementary oligonucleotides, triggering network formation and a distinct color change from red to purple.[18] This strategy has served as the foundation for numerous Au NP-based colorimetric biosensors.

In non-cross-linking aggregation, bare or unmodified Au NPs are used. Single-stranded DNA (ssDNA) adsorbs onto citrate-capped Au NPs through interactions between the DNA bases and the nanoparticle surface, while the DNA's negative charges enhance electrostatic stabilization. Upon hybridization with complementary DNA, the resulting duplexes exhibit reduced affinity for the Au NP surface, leading to nanoparticle aggregation at optimal salt concentrations and consequent color changes.[18] This mechanism has been successfully implemented in multiple colorimetric biosensors.[21]

In this study, we introduce a novel optical biosensing platform for detecting miR-155, a critical breast cancer biomarker. Building upon the non-cross-linking aggregation principle, our design innovatively employs two oppositely charged Au NPs, with their interactions modulated by the presence of the target miR-155. Specifically, the system employs positively charged polyethylenimine-capped Au NPs (PEI-Au NPs) and negatively charged citrate-capped Au NPs (Cit-Au NPs) functionalized with capture probes. In the absence of the target, electrostatic attraction between the oppositely charged nanoparticles destabilizes the Cit-Au NPs, inducing aggregation and a visible color change. In the presence of miR-155, the target hybridizes with the capture probes on Cit-Au NPs, forming stable double-stranded complexes that resist destabilization by PEI-Au NPs, thereby preserving the original solution color. Critically, unlike conventional non-cross-linking methods that rely on salt-induced aggregation, our approach utilizes positively charged PEI-Au NPs as a signal-amplifying agent, eliminating the need for salt addition.

This charge-modulation-based mechanism enables the development of a highly sensitive and visual colorimetric biosensor for miR-155 detection, offering significant potential for rapid, low-cost breast cancer diagnostics.

2. Experimental

2.1 Chemicals and reagents

All chemicals and reagents were of analytical grade and used without further purification. Polyethylenimine (PEI; 50% aqueous solution, molecular weight ~1200–1300), hydrogen tetrachloroaurate(III) trihydrate ($HAuCl_4 \cdot 3H_2O$), and dialysis tubing were purchased from Sigma-Aldrich (USA). Hydrochloric acid (HCl), trisodium citrate dihydrate ($Na_3C_6H_5O_7 \cdot 2H_2O$), and Tween-20 were obtained from Merck (Germany). The HPLC-purified oligonucleotides included hsa-miR-155 (5′-UUAAUGCUA AUCGUGAUAGGGGU-3′) and a three-base mismatched hsa-miR-155 control sequence (5′-UUAAUGCUUAUCGAGAUACGGGU-3′), both purchased from Bioneer Corporation (South Korea). Additionally, a thiolated miR-155 capture probe (5′-AAAAAAAAA CCCCTATCACGATTAGCATTAATTTTTTTTT-HS-3′) was custom synthesized by AnaSpec, Inc. (Canada).

2.2 Probe immobilization on citrate-capped Au NPs (Cit-Au NPs/probe)

The thiolated probe was covalently immobilized onto citrate-capped gold nanoparticles (Cit-Au NPs) through a multi-step procedure. First, 20 nm Cit-Au NPs were synthesized *via* the trisodium citrate reduction method.[22] Briefly, 3 mL of 1% (w/v) trisodium citrate solution was rapidly injected into 40 mL of a boiling 0.8 mM $HAuCl_4$ solution under vigorous stirring. The reaction mixture was maintained at boiling for an additional 20 minutes, yielding a stable, wine-red colloidal solution.

For probe conjugation, 800 μL of the synthesized Cit-Au NP solution was mixed with 800 μL of 1 μM thiolated probe in the presence of Tween 20. The mixture was incubated at room temperature for 48 hours to facilitate complete thiol–gold bond formation. After incubation, the solution was centrifuged to pellet the nanoparticles. The resulting oily red precipitate was carefully resuspended in 400 μL of deionized water to yield the final probe-functionalized Cit-Au NPs (Cit-Au NPs/probe).

2.3 Synthesis of polyethylenimine-capped Au NPs (PEI-Au NPs)

PEI-Au NPs were synthesized according to previously reported protocols[23,24] with minor modifications. In a typical synthesis, 200 μL of PEI solution was added to 6 mL of 1.5 mM $HAuCl_4$ under vigorous magnetic stirring. The mixture was then brought to a boil with continuous stirring. Within 15 minutes of heating, the solution color changed from yellow to red, indicating the successful formation of PEI-Au NPs. The resulting nanoparticle suspension was purified by dialysis against deionized water using a 3.5 kDa molecular weight cutoff membrane.

2.4 Characterization

The UV-visible absorption spectra of the nanoparticles were recorded at room temperature using a Varian Cary Bio 100 spectrophotometer. Measurements were performed in 1 cm pathlength quartz cuvettes across the 400–800 nm wavelength range. Particle size distribution and zeta potential were determined by dynamic light scattering (DLS) using a 90 Plus PALS system (Brookhaven Instruments Corp., USA) equipped with PALS zeta potential analysis software. Morphology and particle size were further characterized by scanning electron microscopy (SEM) using a KYKY EM3200 instrument (China). Optical sensing experiments were conducted using a microplate reader (BioTek PowerWave XS2, USA).

2.5 Spike-and-recovery assay in serum

Healthy human serum was obtained from Shahid Sadoughi Hospital (Yazd, Iran). Aliquots of the serum were spiked with synthetic miR-155 at selected concentrations spanning the linear detection range (expressed in attomolar, aM). These spiked samples were processed using the identical assay protocol applied to calibration standards. All measurements were performed in triplicate to ensure reproducibility.

For comparative purposes, the same concentrations of miR-155 were independently assayed in deionized (DI) water under identical experimental conditions. The recovery percentage was calculated using the following equation:

$$\text{Recovery (\%)} = 100 \times \frac{A_{530}/A_{750}\ (\text{serum})}{A_{530}/A_{750}\ (\text{DI water})}$$

2.6 PEI-AuNP concentration determination

Based on the synthesis parameters and assuming spherical nanoparticles with an average diameter of approximately 20 nm, the initial concentration of PEI-AuNPs was estimated to be 5.87×10^{-9} M, equivalent to approximately 3.53×10^{12} particles per mL. During optimization experiments, different volumes of PEI-AuNPs (10, 20, 30, and 40 μL) were added to the reaction mixture. The resulting final concentrations, expressed in both molarity and particle count per milliliter, are summarized in Table S1 for reproducibility.

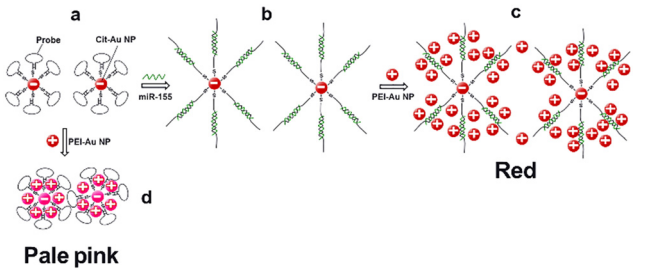

Fig. 1 Schematic of the miR-155 optical detection mechanism: (a) formation of Cit-Au NPs/probe conjugates, (b) introduction of miR-155, (c) addition of PEI-Au NPs in the presence of miR-155 or (d) in the absence of miR-155.

3. Results and discussion

3.1 Detection mechanism of miR-155

The detection mechanism for miR-155 is illustrated in Fig. 1. The process begins with the covalent attachment of a thiolated probe to citrate-stabilized gold nanoparticles (Cit-Au NPs), forming Cit-Au NPs/probe conjugates (Fig. 1a). The probe is designed with nine adenine nucleotides at the 5′ end and nine thymidine spacers at the 3′ end, promoting optimal surface immobilization and hybridization by forming a stable hairpin structure. The central region of the probe is fully complementary to the target miR-155 sequence.[25] Upon introduction of miR-155 (Fig. 1b), hybridization with the probe disrupts the hairpin conformation. Both the probe and the target miRNA carry negatively charged phosphate backbones.

For miR-155 detection (Fig. 1c), positively charged PEI-Au NPs are introduced, which electrostatically bind to the negatively charged probe–target complex. Two factors contribute to increased interparticle distances, preventing nanoparticle aggregation and generating a distinct colorimetric response: (1) disruption of the hairpin structure upon probe–target hybridization and (2) adsorption of PEI-Au NPs onto the double-stranded probe–target complex. As a result, in the presence of miR-155, the Au NP solution retains its characteristic wine-red color due to nanoparticle dispersion. PEI-Au NPs enhance detection sensitivity *via* their large active surface area and nanoparticle stabilization capacity. The resulting target-induced nanoparticle separation enhances colloidal stability, visually confirmed by the solution's intensified red coloration upon PEI-Au NP addition. In contrast, in the absence of the target (Fig. 1d), the probes maintain their hairpin conformation, allowing closer proximity between Au NPs, leading to partial aggregation, visually manifested as a visible color change from wine-red to pale pink. The detection principle thus relies on electrosteric stabilization — a combination of electrostatic repulsion and steric hindrance — that modulates the plasmonic absorption properties of Au NPs based on the presence or absence of the target.

3.2 Novelty of the biosensing mechanism

This study introduces a significant advancement in miR-155 detection through an innovative nanoparticle-based

biosensing strategy. The mechanism comprises three key steps: (1) immobilization of a thiolated probe onto negatively charged citrate-stabilized gold nanoparticles (Cit-Au NPs), (2) hybridization of the probe with the target miR-155 to form probe–target duplexes on the nanoparticle surface, and (3) introduction of positively charged polyethyleneimine-functionalized Au NPs (PEI-Au NPs), which differentially stabilize or destabilize the system depending on the presence of the target. This design results in distinct colorimetric responses: the solution maintains its wine-red color when the target is present but shifts to pale pink in its absence. Notably, PEI-Au NPs function as effective signal amplifiers within this configuration.

This approach fundamentally differs from our previous work,[27] where both the probe and target were immobilized on oppositely charged Au NPs, and detection relied on nanoparticle aggregation (red-to-pink color change) following duplex formation. In contrast, the current method reverses this colorimetric response and offers several advantages: (1) elimination of target immobilization, (2) reduction of preparation steps, (3) minimal reagent handling, (4) decreased potential for false positives or negatives, and (5) overall simplification of the biosensing procedure. Collectively, these improvements deliver a faster, more reliable, and cost-effective detection platform while maintaining high sensitivity and specificity.

The core innovation lies in the strategic exploitation of electrostatic interactions between the probe–target duplexes and PEI-Au NPs, enhancing system stabilization in the presence of miR-155. This mechanism marks a paradigm shift from traditional aggregation-based detection strategies and highlights the versatility and potential of nanoparticle-mediated biosensing technologies.

3.3 Characterization of Cit-Au NPs and PEI-Au NPs

The positively and negatively charged gold nanoparticles (Au NPs) were synthesized using modified chemical reduction methods as previously described.[26,28] Positively charged polyethylenimine-functionalized Au NPs (PEI-Au NPs) were prepared in the presence of polyethylenimine, while negatively charged citrate-capped Au NPs (Cit-Au NPs) were synthesized using sodium citrate as the reducing and stabilizing agent.

UV-vis spectroscopic analysis (Fig. 2A and E) revealed characteristic surface plasmon resonance (SPR) bands centered around 530 nm for both types of Au NPs, confirming the successful formation of colloidal nanoparticles. Morphological characterization by electron microscopy and DLS demonstrated that both PEI-Au NPs and Cit-Au NPs exhibited a spherical morphology (Fig. 2B and F) with uniform size distributions (Fig. 2C and G). Quantitative analysis determined mean diameters of 20.2 ± 1.4 nm for Cit-Au NPs and 27.7 ± 1.3 nm for PEI-Au NPs.

Zeta potential measurements (Fig. 2D and H) further confirmed the expected surface charge properties: Cit-Au NPs displayed a negative potential of −13.4 ± 0.7 mV, attributed to dicarboxy acetone oxidation products derived from citrate adsorption,[28] whereas PEI-Au NPs exhibited a strongly positive potential of 40.7 ± 1.0 mV due to the protonated amine groups present in the polyethylenimine coating.

3.4 Immobilization of a thiolated probe and miR-155 target on Cit-Au NPs

Fig. 3 presents the UV-vis spectral analysis of Cit-Au NPs/probe conjugates before and after hybridization with the target miR-155, followed by the addition of PEI-Au NPs. The absorption peak of the Au NPs shows a slight increase at approximately 530 nm, accompanied by a modest decrease in absorbance across the 600–800 nm range. These spectral changes provide important insights into the dispersion state of the nanoparticles.

The absorption peak at 530 nm reflects the presence of dispersed Au NPs, while absorbance in the 600–800 nm region is indicative of nanoparticle aggregation.[26] The observed increase in the 530 nm peak intensity, coupled with the reduction in long-wavelength absorbance, suggests enhanced nanoparticle stability and decreased aggregation following the probe–target hybridization and interaction with PEI-Au NPs. This shift in surface plasmon resonance arises

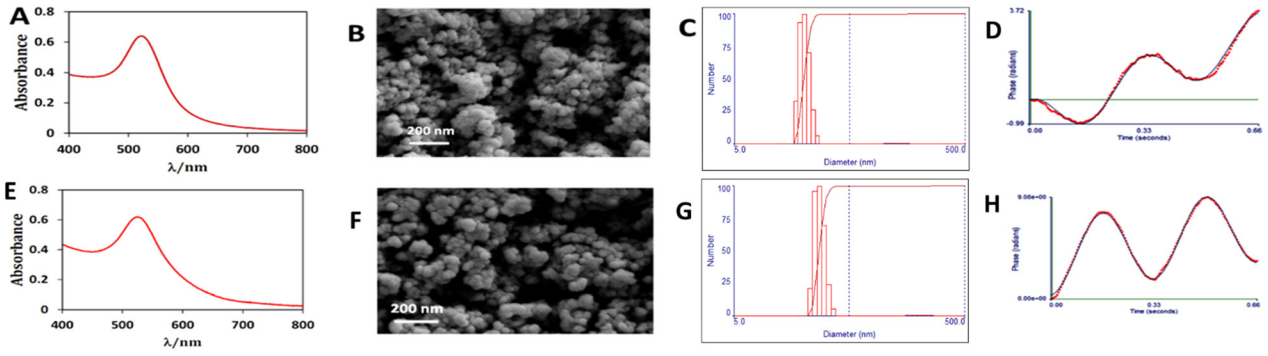

Fig. 2 (A) UV-vis absorption spectrum, (B) SEM image, (C) size-distribution histogram, and (D) zeta potential of Cit-Au NPs. (E) UV-vis absorption spectrum, (F) SEM image, (G) size-distribution histogram, and (H) zeta potential of PEI-Au NPs.

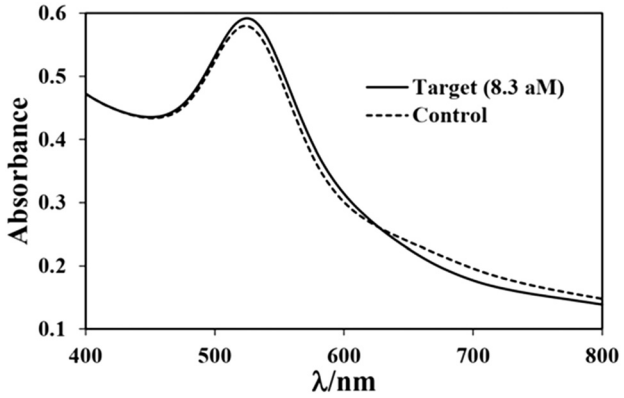

Fig. 3 UV-vis spectra of Cit-Au NPs/probe in the absence (control) and presence of 8.3 aM miR-155.

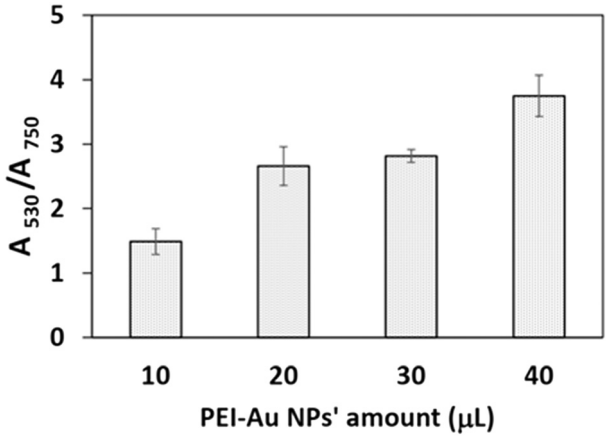

Fig. 4 A_{530}/A_{750} intensities were obtained at different Au-PEI NP concentrations. Each sample also contains 5 μL Au NPs and 8.3 aM miR-155.

from electrosteric interactions, promoting nanoparticle separation and improving colloidal stability.[27]

3.5 Principle of miR-155 detection

The detection principle is based on the characteristic spectral changes observed following probe–target hybridization and subsequent addition of PEI-Au NPs. As described in the previous section, these interactions induce two distinct modifications in the UV-vis absorption profile: an increase in intensity at ~530 nm, corresponding to dispersed nanoparticles, and a decrease in absorbance in the 600–800 nm range, indicative of reduced aggregation. For quantitative analysis, 750 nm was selected as the optimal monitoring wavelength within the aggregation-sensitive region due to its superior measurement reproducibility.

To enhance analytical accuracy, the absorption ratio A_{530}/A_{750} was adopted as a robust parameter, providing greater precision than individual absorbance values.[27] This ratio specifically reflects the molar balance between dispersed and aggregated nanoparticles, with A_{530} representing the surface plasmon resonance of stable Au NPs and A_{750} serving as an indicator of nanoparticle aggregation.[29] The system exhibits a direct correlation between A_{530}/A_{750} values and nanoparticle dispersion: higher ratios indicate enhanced stability, whereas lower ratios reflect increased aggregation.

This relationship enables quantitative detection of miR-155, as the extent of probe–target hybridization modulates electrosteric stabilization effects and thereby influences the A_{530}/A_{750} ratio.[30] Through systematic optimization, we determined that the addition of 40 μL of PEI-Au NPs resulted in the highest A_{530}/A_{750} values (Fig. 4). This optimized condition was employed throughout all subsequent experiments to ensure consistent and reliable detection performance.

3.6 Calibration curve for the detection of miR-155

As shown in Fig. 5, the biosensing platform described in Fig. 1 was used to detect varying concentrations of miR-155. A calibration curve was constructed by plotting the A_{530}/A_{750} absorption ratio against the logarithm of miR-155 concentration. The resulting curve displayed a sigmoidal profile, with a linear dynamic range spanning approximately 80 pM to 2 μM (Fig. 5, inset).

The presented assay achieves an exceptionally broad detection range, spanning from attomolar to micromolar concentrations of miR-155, which is rarely reported in miRNA biosensors. Owing to this wide range, the overall calibration curve exhibits a sigmoidal profile, which can be mechanistically interpreted as follows:

(1) At higher target concentrations, surface saturation of probe-functionalized AuNPs leads to a plateau in signal response, analogous to Langmuir-type adsorption behavior, where binding sites are fully occupied.[31]

(2) In the intermediate concentration range, cooperative hybridization and plasmonic coupling between nanoparticles produce a steep, highly sensitive response, described by classical cooperative binding models such as the Hill equation.[32]

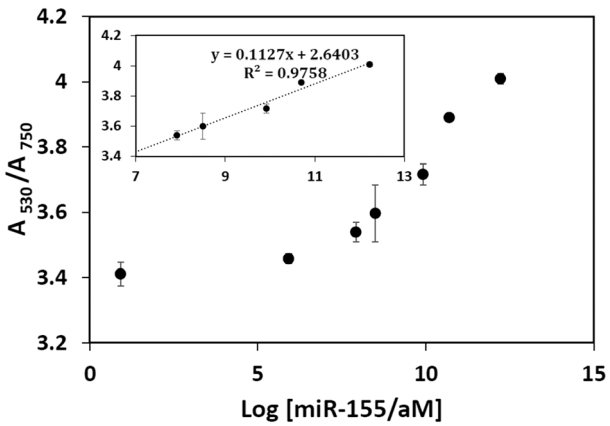

Fig. 5 Calibration curve for the determination of miR-155; the inset shows the linear range of the calibration curve.

(3) At ultra-low concentrations (attomolar), the assay achieves signal amplification through the electrostatic recruitment of PEI-AuNPs by the negatively charged probe–target complex, enabling detectable signals well below conventional LODs.[27]

To ensure robust quantification, we apply logarithmic scaling (log[miR-155]) and confine linear regression analysis to the quantitative dynamic range (approximately 80 pM to 2 μM), where the biosensor response demonstrates optimal reliability.

The limit of detection (LOD) was estimated to be ~8 pM, determined by identifying the intersection point of the maximum and minimum slope tangents at low concentrations.[27]

Although the limit of detection (LOD) determined from the calibration curve is approximately 8 pM, a detectable colorimetric response was observed at lower concentrations, including 8.3 aM (Fig. 3). This apparent discrepancy stems from the detection mechanism inherent to the biosensor. The LOD, calculated using established statistical criteria, represents the lowest concentration at which the analyte can be reliably quantified above background noise. In contrast, the signal observed at 8.3 aM reflects a qualitative detection enabled by localized surface amplification effects. At ultralow concentrations, three mechanisms enhance sensitivity: (i) surface-localized enrichment of miR-155 on probe-functionalized AuNPs significantly increases the local effective concentration. (ii) Electrostatic recruitment of PEI-AuNPs amplifies interparticle spacing changes, enhancing signal contrast; and (iii) plasmonic coupling effects produce a nonlinear optical response that allows detection of signals below the quantitative LOD.

Consequently, while the calibration curve defines the quantitative dynamic range (80 pM to 2 μM), the system can still provide qualitative evidence of miR-155 presence at concentrations below the LOD due to the localized surface amplification effects.

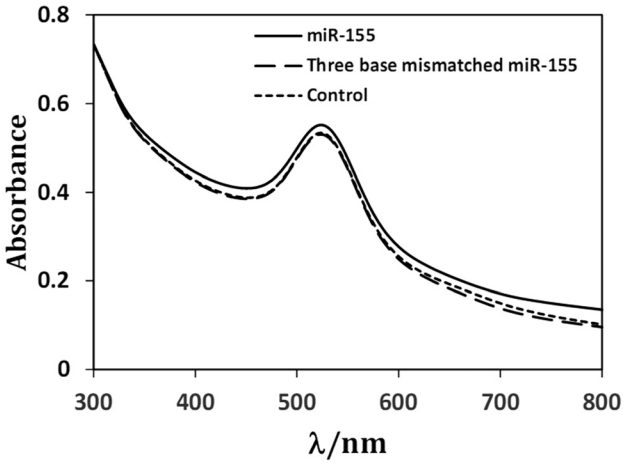

Fig. 6 Selectivity of the biosensor toward miR-155 in comparison with three base mismatched miR-155. The concentration of miR-155 and three base mismatched miR-155 in samples was 5×10^{10} aM.

3.7 Selectivity assessment of the miR-155 biosensor

The selectivity of the miR-155 biosensor was evaluated by comparing its response to three different samples: (1) the perfectly matched miR-155 target, (2) a three-base mismatched sequence, and (3) probe-conjugated citrate-capped Au NPs (Cit-Au NPs/probe) alone as a negative control. As shown in Fig. 6, the system exhibited the highest A_{530}/A_{750} value in the presence of the fully complementary miR-155 target. In contrast, both the mismatched target and the negative control produced significantly lower signals, which were essentially indistinguishable from one another. This clear differentiation underscores the biosensor's high sequence specificity. All samples, including controls, were tested under identical conditions with the same concentration of PEI-Au NPs to ensure experimental consistency. The observed selectivity profile demonstrates the platform's strong ability to distinguish the target miRNA from closely related sequences with minimal cross-reactivity.

3.8 Evaluation of anti-interference capability in serum

To evaluate the effect of biological matrices, we evaluated the response of the biosensor to two representative concentrations of miR-155 spiked into healthy human serum and compared the responses with those obtained from control samples containing the same miR-155 concentrations dissolved in deionized (DI) water. All concentrations are expressed in attomolar (aM) units.

For instance, a log[miR-155] value of 9.91 corresponds to a concentration of approximately 8.3×10^9 aM (~8.3 nM). At this concentration, the biosensor exhibited an A_{530}/A_{750} ratio of 3.09 ± 0.15 in human serum, compared to 3.71 ± 0.03 in deionized (DI) water, yielding a recovery rate of approximately 83.3%.

Similarly, at log[miR-155] = 7.91 (equivalent to $\sim 8.1 \times 10^7$ aM or ~81 pM), the biosensor's A_{530}/A_{750} ratio was 2.88 ± 0.16 in serum *versus* 3.53 ± 0.03 in DI water, corresponding to a recovery of approximately 81.6%.

The recovery values fall within the widely accepted range of 80–120%, indicating that serum matrix components induce only minimal signal suppression at the tested concentrations.

Conclusions

We have successfully developed a novel biosensing platform for miR-155 detection that integrates cost-effectiveness, rapid analysis, and high sensitivity. The detection mechanism involves a sequential process beginning with the hybridization of the target miR-155 to probe-functionalized citrate-capped gold nanoparticles (Cit-Au NPs), followed by the addition of positively charged polyethyleneimine-coated gold nanoparticles (PEI-Au NPs), which induces measurable changes in the surface plasmon resonance (SPR) absorption profile. The quantitative basis of this approach lies in concentration-dependent electrosteric interactions between

the negatively charged Cit-Au NP–probe/target complexes and the positively charged PEI-Au NPs. Our experimental results clearly demonstrate that PEI-Au NPs function as highly effective signal amplifiers, significantly enhancing the sensitivity of gold nanoparticle-based biosensing systems. Additionally, the large surface area of the PEI-Au NPs—attributable to the polyethyleneimine coating—further contributes to the system's improved sensitivity. This innovative use of electrosteric stabilization between oppositely charged nanoparticles offers a robust foundation for the future development of nanoparticle-based biosensors. The platform's unique combination of technical performance and practical accessibility makes it particularly well-suited for both research and clinical diagnostic applications where accurate and efficient miRNA detection is essential.

Author contributions

Conceptualization and methodology were done by F. H.; data analysis and investigation were provided by B. D. and V. S.; writing – the original draft was prepared by S. H. and F. D.; writing – review and editing were performed by H. G., M. B. R., H. F. and F. H.; supervision was conducted by H. G.

Conflicts of interest

The authors declare no competing financial interests.

Data availability

Supplementary information is available. See DOI: **https://doi.org/10.1039/D5SD00129C**.

Data for this article, including UV-vis spectra datasets are available at **https://doi.org/10.6084/m9.figshare.29580617**.

Notes and references

1 J. Huang, S. Yu, L. Ding, L. Ma, H. Chen, H. Zhou, Y. Zou, M. Yu, J. Lin and Q. Cui, *Biomedicines*, 2021, **9**, 1590.
2 A. M. Grimaldi, M. Salvatore and M. Incoronato, *Front. Oncol.*, 2021, **11**, 668464.
3 T. Arancibia, S. Morales-Pison, E. Maldonado and L. Jara, *Biol. Res.*, 2021, **54**, 26.
4 P. Zubor, P. Kubatka, K. Kajo, Z. Dankova, H. Polacek, T. Bielik, E. Kudela, M. Samec, A. Liskova, D. Vlcakova, T. Kulkovska, I. Stastny, V. Holubekova, J. Bujnak, Z. Laucekova, D. Busselberg, M. Adamek, W. Kuhn, J. Danko and O. Golubnitschaja, *Int. J. Mol. Sci.*, 2019, **20**, 2878.
5 P. Zubor, P. Kubatka, Z. Dankova, A. Gondova, K. Kajo, J. Hatok, M. Samec, M. Jagelkova, S. Krivus, V. Holubekova, J. Bujnak, Z. Laucekova, K. Zelinova, I. Stastny, M. Nachajova, J. Danko and O. Golubnitschaja, *Future Oncol.*, 2018, **14**, 1847–1867.
6 C. L. Wong, S. Y. Loke, H. Q. Lim, G. Balasundaram, P. Chan, B. K. Chong, E. Y. Tan, A. S. G. Lee and M. Olivo, *J. Biophotonics*, 2021, **14**, e202100153.
7 R. Bruch, J. Baaske, C. Chatelle, M. Meirich, S. Madlener, W. Weber, C. Dincer and G. A. Urban, *Adv. Mater.*, 2019, **31**, e1905311.
8 A. Miti, S. Thamm, P. Muller, A. Csaki, W. Fritzsche and G. Zuccheri, *Biosens. Bioelectron.*, 2020, **167**, 112465.
9 J. Xu, K. J. Wu, Q. J. Jia and X. F. Ding, *J. Zhejiang Univ., Sci., B*, 2020, **21**, 673–689.
10 J. S. Wong and Y. K. Cheah, *Noncoding RNAs*, 2020, **6**, 29.
11 A. R. Cardoso, F. T. C. Moreira, R. Fernandes and M. G. F. Sales, *Biosens. Bioelectron.*, 2016, **80**, 621–630.
12 W. Kong, L. He, E. J. Richards, S. Challa, C. X. Xu, J. Permuth-Wey, J. M. Lancaster, D. Coppola, T. A. Sellers, J. Y. Djeu and J. Q. Cheng, *Oncogene*, 2014, **33**, 679–689.
13 Z. Sun, Y. Tong, X. Zhou, J. Li, L. Zhao, H. Li, C. Wang, L. Du and Y. Jiang, *ACS Omega*, 2021, **6**, 34150–34159.
14 S. Panneerselvam and S. Choi, *Int. J. Mol. Sci.*, 2014, **15**, 7158–7182.
15 K. Akshaya, C. Arthi, A. J. Pavithra, P. Poovizhi, S. S. Antinate, G. S. Hikku, K. Jeyasubramanian and R. Murugesan, *Photodiagn. Photodyn. Ther.*, 2020, **30**, 101699.
16 R. Zhu, J. Song, Y. Zhou, P. Lei, Z. Li, H.-W. Li, S. Shuang and C. Dong, *Talanta*, 2019, **204**, 294–303.
17 D.-K. Nguyen and C.-H. Jang, *Micromachines*, 2021, **12**, 1526.
18 E. Shokri, M. Hosseini, M. D. Davari, M. R. Ganjali, M. P. Peppelenbosch and F. Rezaee, *Sci. Rep.*, 2017, **7**, 45837.
19 J. Cai, L. Ding, P. Gong and J. Huang, *Nanotechnology*, 2019, **31**, 095501.
20 G. Wang, Y. Akiyama, S. Shiraishi, N. Kanayama, T. Takarada and M. Maeda, *Bioconjugate Chem.*, 2017, **28**, 270–277.
21 F. Zhang and J. Liu, *Analysis Sensing*, 2021, **1**, 30–43.
22 X. Ji, X. Song, J. Li, Y. Bai, W. Yang and X. Peng, *J. Am. Chem. Soc.*, 2007, **129**, 13939–13948.
23 F. S. Mohammed, S. R. Cole and C. L. Kitchens, *ACS Sustainable Chem. Eng.*, 2013, **1**, 826–832.
24 X. Sun, X. Jiang, S. Dong and E. Wang, *Macromol. Rapid Commun.*, 2003, **24**, 1024–1028.
25 C. Pöhlmann and M. Sprinzl, *Anal. Chem.*, 2010, **82**, 4434–4440.
26 F. Hakimian and H. Ghourchian, *Mater. Sci. Eng., C*, 2019, **103**, 109795.
27 F. Hakimian, H. Ghourchian, A. S. Hashemi, M. R. Arastoo and M. Behnam Rad, *Sci. Rep.*, 2018, **8**, 2943.
28 P. Zhao, N. Li and D. Astruc, *Coord. Chem. Rev.*, 2013, **257**, 638–665.
29 S.-J. Chen, Y.-F. Huang, C.-C. Huang, K.-H. Lee, Z.-H. Lin and H.-T. Chang, *Biosens. Bioelectron.*, 2008, **23**, 1749–1753.
30 K. Wagers, T. Chui and S. Adem, *IOSR J. Appl. Chem.*, 2014, **7**, 15–20.
31 K. Melgarejo, M. del Barrio, E. Benito-Peña, T. Mirea and C. A. Barrios, *Plasmonics*, 2025, **1**, 1.
32 G. Ghotra, N. H. Le, H. Hayder, C. Peng and J. I. Chen, *Can. J. Chem.*, 2021, **99**, 585–593.